Weierstraß-Institut
für Angewandte Analysis und Stochastik

Leibniz-Institut im Forschungsverbund Berlin e. V.

Preprint ISSN 2198-5855

Time-dependent simulation of thermal lensing in high-power broad-area semiconductor lasers

Anissa Zeghuzi[1], Hans-Jürgen Wünsche[1,2], Hans Wenzel[1], Mindaugas Radziunas[2], Jürgen Fuhrmann[2], Andreas Klehr[1], Uwe Bandelow[2], Andrea Knigge[1]

submitted: October 17, 2019

[1] Ferdinand-Braun-Institut
Leibniz Institut für Höchstfrequenztechnik
Gustav-Kirchhoff-Straße 4
12489 Berlin
Germany
E-Mail: anissa.zeghuzi@fbh-berlin.de
hans-juergen.wuensche@fbh-berlin.de
hans.wenzel@fbh-berlin.de
andreas.klehr@fbh-berlin.de
andrea.knigge@fbh-berlin.de

[2] Weierstrass Institute
Mohrenstr. 39
10117 Berlin
Germany
E-Mail: hans-juergen.wuensche@wias-berlin.de
mindaugas.radziunas@wias-berlin.de
juergen.fuhrmann@wias-berlin.de
uwe.bandelow@wias-berlin.de

No. 2634
Berlin 2019

2010 *Mathematics Subject Classification.* 78A60, 35Q60, 78-04, 70K70, 35Q79, 81Q37.

Key words and phrases. Broad-area laser, heat flow, pulsed laser operation, traveling-wave model, thermal lensing, temperature fluctuation.

This work has been supported by the German Federal Ministry of Education and Research (BMBF) contract 13N14005 as part of the EffiLas/HoTLas project. Furthermore we thank A. Pietrzak (JENOPTIK Optical Systems) for providing laser chips and K. Häusler and M. Beier for measurements.

Edited by
Weierstraß-Institut für Angewandte Analysis und Stochastik (WIAS)
Leibniz-Institut im Forschungsverbund Berlin e. V.
Mohrenstraße 39
10117 Berlin
Germany

Fax: +49 30 20372-303
E-Mail: preprint@wias-berlin.de
World Wide Web: http://www.wias-berlin.de/

Time-dependent simulation of thermal lensing in high-power broad-area semiconductor lasers

Anissa Zeghuzi, Hans-Jürgen Wünsche, Hans Wenzel, Mindaugas Radziunas, Jürgen Fuhrmann, Andreas Klehr, Uwe Bandelow, Andrea Knigge

Abstract

We propose a physically realistic and yet numerically applicable thermal model to account for short and long term self-heating within broad-area lasers. Although the temperature increase is small under pulsed operation, a waveguide that is formed within a few-ns-long pulse can result in a transition from a gain-guided to an index-guided structure, leading to near and far field narrowing. Under continuous wave operation the longitudinally varying temperature profile is obtained self-consistently. The resulting unfavorable narrowing of the near field can be successfully counteracted by etching trenches.

1 Introduction

Due to their small size and high efficiency broad-area (BA) lasers are important pump sources for high-performance laser systems and also used for direct material processing. Tens of watts output from single devices can be obtained. Accordingly, a large amount of heat is generated. Even being cooled, the interior temperature is increased with large impact on the laser operation. The most prominent effect is the formation of a thermally induced waveguide, i.e. a substantial increase of the refractive index in the hot center below the contact stripe (cf. Fig. 1) commonly referred to as thermal lensing. This effect is well studied both experimentally [1] and theoretically [2, 3, 4] for continuous wave (CW) operation assuming a stationary temperature distribution. It is usually neglected under pulsed operation because thermal build-up times up to milliseconds are much longer than the pulse lengths. However, the heat is generated near to the active layer in the same region where the guided wave is localized. This region is small and its thermal build-up time is much shorter than that of the whole device.

Short-time local heating can be expected to influence the optical pulse formation although time-averaged heating is negligible. Theoretically, a time-dependent temperature has been considered in early models as presented e.g. in Refs. [5, 6]. They concentrated on a sophisticated microscopic description of the processes in the active layer. However, besides requiring enormous computer resources even for nanosecond transients, they disregarded outer parts of devices, where a considerable portion of the heat is generated. Heat flow was replaced by a simple local relaxation of temperature towards an ambient temperature. These features prevent an application in device design.

In this paper we present and apply a new time-dependent quasi three-dimensional electro-optic-thermal modeling of BA lasers. A description of the device structure and an experimental motivation for the implementation of short-time heating are given in section 2. The electro-optical and thermal models are introduced in sections 3 and 4, respectively. Exemplary laser operation with 10 ns long pulses is simulated in section 5, revealing a fast-growing thermally induced waveguide initializing the known stationary thermal lense. The application of the time-dependent approach to CW operation in

DOI 10.20347/WIAS.PREPRINT.2634 Berlin 2019

section 6 yields strong spatio-temporal sub-ns fluctuations of the heat sources. However, they have a negligible influence on the wave propagation, whereas the effects of the time-averaged londitudinally varying temperature profile confirm those obtained with stationary temperatures in a previous publication [7]. It is shown how these effects can be tailored by appropriate lateral trenches. Furthermore simulation results are validated by measurements. The paper is summarized in section 7.

2 Studied device structure and experimental motivation

The simulated device sketched in Fig. 1 is representative for high-power BA lasers. It has a cavity length of $L = 4$ mm, a width of the contact stripe of $W = 100\,\mu$m, and rear and front facet power reflectivities of $R_0 = 0.95$ and $R_L = 0.01$, respectively. The active layer consists of a 7 nm thick single InGaAs quantum well (QW) embedded in p- and n-doped $Al_xGa_{1-x}As$ layers with thicknesses d and Al mol fractions x chosen to eliminate carrier accumulation largely (n-cladding: $d = 1.5\,\mu$m, $x = 0.35$, n-confinement: $d = 2.54\,\mu$m, $x = 0.35 \to 0.2$, p-confinement: $d = 0.25\,\mu$m, $x = 0.2 \to 0.7$, p-cladding: $d = 0.63\,\mu$m, $x = 0.7$, p-GaAs cap: $d = 0.83\,\mu$m). To provide lateral current confinement the p-doped layers are implanted down to the vicinity of the active region, rendering these areas highly resistive.

Experimental evidence of short time local heating is visible in Fig. 2 and can also be found in e.g. Ref. [8]. The lateral aperture of the experimentally investigated laser in Fig. 2 is defined by an etched mesa with a width of 100 μ m. It is operated with a 25 ns long pulse and a low pulse repetition rate of 10 kHz in order to exclude heating between the pulses. Details on the experimental setup can be found in [9]. After relaxation the center wavelength starts shifting to longer wavelength as a result of self-heating in and around the active region. As a consequence, short-time local heating might become relevant. These arguments hold particularly under short-pulse operation when hundreds of ampere flow during only few nanoseconds with typically tens of microseconds rest period between the pulses.

3 Optical and electrical model

Our mathematical model is a hybrid combination of (A) a traveling-wave (TW) model in the (x, z) plane, (B) a model of current flow in the (x, y) plane, and (C) a thermal model. In this section, (A) and (B) are sketched only briefly (more details in Appendix A). We focus on their connection with the thermal extension (C). For brevity, dependencies on time t and position (x, y, z) will be mentioned only where important.

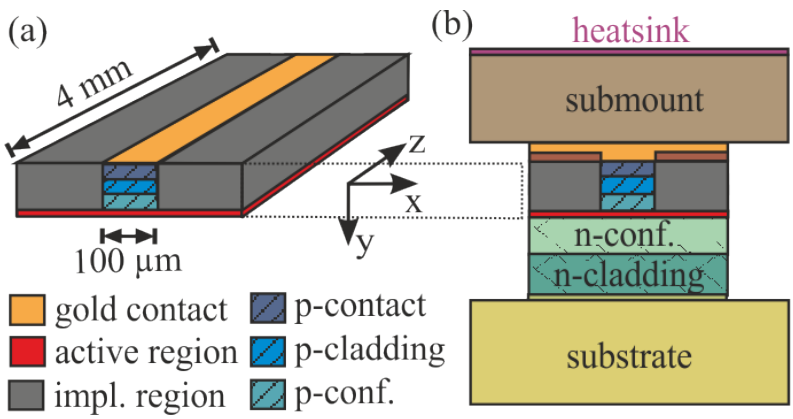

Figure 1: Sketches of a typical BA laser. (a) Domain of the electro-optical simulation. (b) Vertical-lateral cross section of the thermal simulation domain.

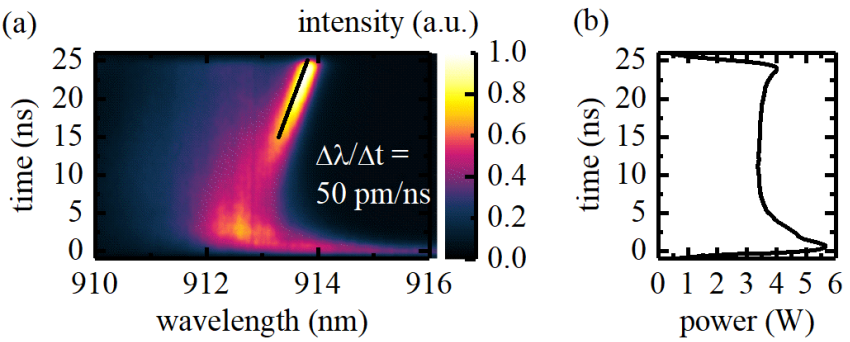

Figure 2: Time evolution of the (a) emission spectra and (b) emitted optical power of a laser operated with 25 ns long pulses at an injection current of 6.3 A and repetition rate of 10 kHz (measured with a streak camera and averaged over 100 shots). The black line in (a) indicates a linear fit of the maximum wavelength as function of time with the wavelength shift $\Delta\lambda/\Delta t = 50$ pm/ns.

3.1 The (x, z) traveling wave model

In the semiclassical framework of rotating-wave, scalar, effective-index and paraxial approximations, the transverse-electric optical field is represented by its electric x-component

$$E(\vec{r},t) = A\,\phi(y)\left[u^{+}\mathrm{e}^{-i\bar{n}k_0 z} + u^{-}\mathrm{e}^{i\bar{n}k_0 z}\right]\mathrm{e}^{i\omega t} + c.c. \tag{1}$$

with $A = \sqrt{d\hbar\omega/(2\epsilon_0\bar{n}n_g)}$ and $k_0 = 2\pi/\lambda_0$. $\lambda_0 = 910$ nm, $d = 7$ nm, $\hbar$, ϵ_0, $n_g = 3.87$, $\bar{n} = 3.4$, ω and c are the center wavelength, the thickness of the active region, the Planck constant, the vacuum permittivity, the group refractive index, a real valued reference index, a reference angular frequency and the vacuum speed of light, respectively. Supposing a well-designed vertical waveguide, the normalized fundamental vertical mode $\phi(y)$ is calculated in advance for the cold cavity and remains unchanged. The slowly varying complex amplitudes $u^{\pm}(x,z,t)$ obey a traveling wave equation (TWE) coupled to a diffusion equation for the carrier density $N(x,z,t)$ (sheet density divided by the QW thickness)

$$\left[\frac{1}{v_\mathrm{g}}\frac{\partial}{\partial t} \pm \frac{\partial}{\partial z} + \frac{i}{2\bar{n}k_0}\frac{\partial^2}{\partial x^2} + \mathcal{D}\right] u^{\pm} = -i\Delta\beta(N,T,\|u\|^2)u^{\pm} + f_\mathrm{sp}^{\pm}, \tag{2}$$

$$\frac{\partial N}{\partial t} = \frac{\partial}{\partial x}\left(D_\mathrm{eff}(N)\frac{\partial N}{\partial x}\right) + \frac{j}{ed} - R(N,\|u\|^2), \tag{3}$$

with the injection current density $j(x,z,t)$, the recombination rate R (see Appendix A), and the photon density

$$\|u\|^2 = |u^{+}(x,z,t)|^2 + |u^{-}(x,z,t)|^2. \tag{4}$$

The group velocity is given by $v_\mathrm{g} = c/n_\mathrm{g}$. The amplitudes $u^{\pm}$ are coupled to each other by reflecting boundary conditions at the facets. Periodic boundary conditions are assumed at the lateral boundaries of the sufficiently broad simulation domain. The dispersion operator $\mathcal{D}$, the spontaneous emission contribution f_sp, and the numerical treatment of the traveling wave equations are described in detail in Ref. [10]. The complex propagation parameter (in excess of $k_0\bar{n}$)

$$\Delta\beta(N,T,\|u\|^2) = \Delta\beta_\mathrm{oe}(N,\|u\|^2) + k_0\Delta n_T(T) \tag{5}$$

is composed of an optoelectronic part given in Ref. [11] (cf. Appendix A) and a thermal contribution $k_0 \Delta n_T$. The real part of $\Delta\beta$ determines the effective index (in excess of $\bar{n}$),

$$\Delta n_{\text{eff}} = \text{Re}(\Delta\beta)/k_0, \tag{6}$$

whereas its imaginary part is the net gain (see (A.1) in Appendix A). The linearized thermally induced index shift

$$\Delta n_T(T) = \int n'_T \cdot (T - T_{\text{HS}})|\phi|^2 dy. \tag{7}$$

with the heat-sink temperature T_{HS} and slope parameter $n'_T = 2.4 \cdot 10^{-4}$ K^{-1} describes the thermal impact on the lateral waveguiding. Note: it does not depend on the local temperature but only on its vertical average, weighted with the mode profile $|\phi(y)|^2$. Hot carriers don't contribute because relaxation times are much shorter than life times or pulse lengths. Fermi distribution functions are also calculated with the lattice temperature T, whereas the material parameters are kept temperature-independent to distinguish thermal waveguiding effects from effects resulting from the dependence of parameters on temperature.

The numerical integration of the TWE model is the computationally most expensive part of our numerical modeling. For this reason, we exploit the software kit `BALaser` [12] which is based on the split-step along the characteristics method for Eq. (3) and the finite difference approximations of Eq. (2). To rapidly solve the discrete large scale problem (2000×800 spatial mesh corresponding to $\Delta x = 0.2\,\mu$m and $\Delta z = 5\,\mu$m lateral and longitudinal discretization steps), the numerical algorithm was parallelized using the distributed-memory paradigm. As a consequence, instead of ~ 3.5 hours required for a simulation of $\sim 1.5 \cdot 10^4$ time iterations corresponding to 1 ns long transients of a typical BA laser using the single process on a single core of our server, we perform the same simulations exploiting 30 processes of the multicore server in about 10 minutes. More details on the numerical algorithm, its parallelization and efficiency can be found in Refs. [10, 13].

3.2 The (x, y) current flow model

Current spreading and current self-distribution in the p-doped layers play an important role in BA lasers [11, 14]. They are also expected to have a large impact on the Joule heating, which is proportional to the square of the current density,

$$\vec{j}_p = \sigma \nabla \varphi_p \tag{8}$$

with the electrical conductivity σ. The quasi-Fermi potential φ_p of the holes is determined by solving a Laplace equation in the p-doped region [15, 14].

$$\nabla(\sigma \nabla \varphi_p) = 0 \tag{9}$$

with the boundary conditions $\varphi_p|_{y=y_a} = \varphi_F(N,T)$, $\varphi_p = U$ at the p-contact, and $\frac{\partial}{\partial n}\varphi_p = 0$ elsewhere, where $\frac{\partial}{\partial n}$ is the normal derivative. U is the bias voltage and $\varphi_F(N,T)$ is the Fermi voltage in the active layer, i.e. the separation between the quasi-Fermi potentials of holes and electrons. The injection current density $j(t,x,z)$ entering Eq. (3) is the y-component of $\vec{j}_p$ at the upper boundary of the active layer adjacent to the p-doped region. We note, that the application of the inhomogeneous current spreading model with each time iteration causes about 50% slow-down of our calculations.

4 Heat Model

The heat model calculates the heat generation using results of the opto-electronic model, solves the heat-flow equation, and determines the thermal index contribution (7) acting on the wave propagation.

4.1 Heat generation model

Heat generation in a semiconductor laser is due to various relaxation processes with a wide span of time scales [5, 6, 16]. Electrons, holes and phonons equilibrate to a common temperature T within picoseconds or less, which is by orders of magnitude shorter than life times or pulse duration. Accordingly, it is adequate to consider relaxation processes as instantaneous, characterized by the amount h of energy per unit time and unit volume transferred to the thermalized system. In what follows we list the heat sources of the model derived from corresponding expressions given in [17, 18].

The Joule heat is

$$h_{\mathsf{J}} = j_p^2/\sigma \tag{10}$$

in the p-doped region and neglected in the n-doped region due to the very high electron conductivity (in accordance with the current flow model).

The heat source due to absorption of stimulated emitted photons is given as

$$h_{\mathsf{abs}} = \begin{cases} v_g\hbar\omega d\alpha_0(y)\frac{n(y)}{\bar{n}}|\phi(y)|^2\|u(x,z,t)\|^2 \\ +(v_g\hbar\omega d)^2\beta_{\mathsf{2P}}(y)\frac{n(y)}{\bar{n}}|\phi(y)|^4\|u(x,z,t)\|^4 \\ \text{for } y \notin \text{active region,} \\ v_g\hbar\omega f_N N\|u(x,z,t)\|^2 \text{ for } y \in \text{active region} \end{cases} \tag{11}$$

where $n(y)$, $\alpha_0(y)$ and $\beta_{\mathsf{2P}}(y)$ denote the vertical distribution of the real part of the refractive index, the absorption and the two-photon absorption coefficient, respectively. The first term in Eq. (11) accounts for background absorption due to doping, the second term denotes two-photon absorption in the cladding and confinement layers and the third term is due to free carrier absorption in the active region. Note that for $\alpha_{0,\mathsf{eff}}$ and f_{2P} entering the effective absorption coefficient of the traveling wave equation (A.2), $\alpha_{0,\mathsf{eff}} = \int n(y)\alpha_0(y)/\bar{n}|\phi|^2 dy$ and $f_{\mathsf{2P}} = \hbar\omega v_g d_a \int n(y)\beta_{\mathsf{2P}}(y)/\bar{n}|\phi|^4 dy$ must hold.

The third source term is recombination heat in the active region,

$$h_{\mathsf{rec}} = e\varphi_F(N,T)(AN + \xi BN^2 + CN^3) \tag{12}$$

where ξ denotes the portion of absorbed spontaneous emission. By setting $\xi = 1$ we have assumed, that all spontaneous emission is transferred into heat within the active region.

This is an overestimation because spontaneously emitted photons are reabsorbed anywhere in the device or leave it. However, a detailed model is unnecessary because far above threshold this heat contributes only to a small amount and the vertical distribution of heat sources only marginally influences the lateral temperature profile [19].

The last term taken into account denotes quantum defect heat generated in the active region as a result of an incomplete energy transfer from the carrier reservoir to the radiation field and is given as

$$h_{\mathsf{defect}} = (e\varphi_F(N,T) - \hbar\omega)R_{\mathsf{stim}}(N, \|u\|^2). \tag{13}$$

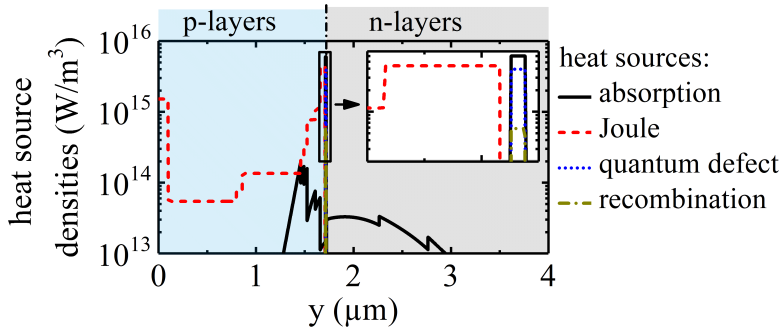

Figure 3: Time averaged absorption, Joule, recombination and quantum defect heat source densities as function of the vertical y-direction for a 10 ns long 150 A current pulse at the front facet in the middle of the stripe.

There is additionally Thompson-Peltier heat [17, 18] generated by a current flow in the presence of gradients of the Seebeck coefficients. However, any temperature gradients would act back on the currents (Seebeck effect), resulting in a major alteration of the electric model. In this paper we set the Seebeck coefficients to zero to keep consistency as the overall impact would be small if accounted for (cf. Appendix B).

4.2 Modeling heat flow

Our model bases on the classical macroscopic heat-flow equation

$$c_{\mathsf{h}} \frac{\partial T}{\partial t} - \nabla \left[\kappa_{\mathsf{L}} \nabla T\right] = h(N, \vec{j}, \|u\|^2), \tag{14}$$

with the heat capacity c_{h} and the heat conductivity κ_{L} (values taken from [20]). The heat source

$$h = h_{\mathsf{J}} + h_{\mathsf{abs}} + h_{\mathsf{rec}} + h_{\mathsf{defect}}, \tag{15}$$

consists of the individual heat sources given in Eqs. (10) - (13). The boundary conditions are

$$\begin{array}{rcll} \kappa_L \frac{\partial}{\partial n} T & = & -(T - T_{\mathsf{HS}})/r_{\mathsf{th}} & \text{for } (x,y,z) \in \text{heat sink} \\ \frac{\partial}{\partial n} T & = & 0 & \text{for } (x,y,z) \in \text{other outer bounds} \end{array} \tag{16}$$

where $r_{\mathsf{th}} = 8.33 \cdot 10^{-6}$ Km^{2}W^{-1} is the inverse heat transfer coefficient. Here and in what follows, T is the absolute temperature and $T_{\mathsf{HS}} = 300$ K the temperature of the heat sink, which also serves as reference for parameter values. The arguments of h on the right hand side of Eq. (14) symbolize that the heat source power density h depends on the carrier density, current density, and field intensity distributions in the laser, which result from the opto-electronic model. Reversely, T acts back on the wave propagation mainly via the thermally induced effective index (7). In addition, T implicitly influences the gain, distribution functions, and the diffusion as well as recombination terms in Eq. (3). Explicit thermal changes are only considered in the Fermi function under CW operation. Thermal changes of parameters are disregarded in order to separate those from thermal waveguiding effects.

4.2.1 The no-heat-flow (NHF) approximation

It is unreasonable to solve the heat-flow equation (14) over tens of microseconds with the sub-ps temporal resolution of the opto-electronic model in the large spatial domain sketched in Fig. 1(b). Fortunately, the following inherent traits of heat generation and conduction enable us to simplify the

problem considerably. During a given time τ, heat generated at a certain position flows only into a finite region of size l which is related to τ by the inverse thermal diffusivity (see also Appendix C)

$$\frac{\tau}{l^2} \approx \frac{c_h}{\kappa_L} \approx 10^5 \text{ s/m}^2 \approx \frac{1 \text{ ns}}{(100 \text{ nm})^2}. \tag{17}$$

During a 1 ns simulation interval, the generated heat is spread by only about 100 nm. Thus, transverse heat flow is certainly negligible because this distance is much smaller than transverse inhomogeneities of the heat source density (Fig. 10). Furthermore, this small-distance redistribution of heat does only marginally affect the thermally induced (effective) index (7), which is a vertical average with the weight function $|\phi(y)|^2$ having a much wider spread. It is this index but not the local temperature, which determines the thermal contribution to lateral waveguiding. Heat flow is therefore negligible when simulating wave guiding during short transients. Differentiating (7) with respect to time and inserting (14) with $\kappa_L = 0$, we find the ordinary differential equation

$$\frac{\partial \Delta n_T}{\partial t} = \int \frac{n_T'}{c_\mathsf{h}} |\phi(y)|^2 h(N, \vec{j}, \|u\|^2) dy \tag{18}$$

for the thermally induced index. At a given instant t, the actual distribution of local heat sources has to be inserted here. Accordingly, this is one equation for the temporal variation of Δn_T in each point (x, z) of the lateral-longitudinal plane. It is integrated much easier in each node of the spatial grid than the original partial differential heat-flow equation (14). The price to pay is no information about the true temperature profile, see the discussion at the end of section 5. Therefore, all parameters of the model including occupation probabilities are derived for the heat-sink temperature $T = T_\mathsf{HS}$. This limits the NHF approximation to short pulses.

4.2.2 Treatment of CW operation

The extremely long thermal build-up in the case of CW operation cannot be calculated with the NHF approximation. But in the later quasi-steady state, the rate of heat generation can be decomposed in a time-constant mean contribution $\bar{h}$ and a contribution $h_\mathsf{fluct} = h - \bar{h}$ fluctuating around zero. h is the total instantaneous heat production (15). Accordingly, the heat-flow equation (14) is split into

$$0 = \nabla \kappa_L \nabla \bar{T} + \bar{h} \qquad \text{and} \tag{19}$$

$$c_h \frac{\partial T_\mathsf{fluct}}{\partial t} = \nabla \kappa_L \nabla T_\mathsf{fluct} + h_\mathsf{fluct} \tag{20}$$

with boundary conditions following from (16) and $\bar{T}$ denoting time-averaged temperature. Obviously, the sum of the two temperatures obeys the full heat-flow equation (14).

The time scale of the fluctuations $h - \bar{h}$ is typically in the sub-ns range. Thus, Eq. (20) is solved with the NHF approximation (18) along a few-ns-long simulation interval. Treating the stationary Eq. (19) is more challenging because heat flow dominates and, in general, it must be solved in the full 3-D domain including submout and substrate. In our study, however, we neglect the longitudinal heat flow component and solve the static problem (19) within multiple ($L/\Delta z = 800$ in our case) lateral-vertical (x-y) cross sections, see Fig. 1(b). Furthermore, the mean heat production $\bar{h}(x, y, z)$ as a function of the coordinates is not known in advance. Therefore, we apply an iterative approach. In the first step of the iteration the electro-optic model is solved under isothermal conditions with $T = T_\mathsf{HS}$. During this run, we set $\bar{h} = 0$. In all following iterations, $\bar{h}$ is taken as the temporal average of the total heat production of the last part of the iteration before and the fluctuating part inserted into (18) is

$h_{\text{fluct}} = h - \bar{h}$. A detailed description of the numerical implementation is given in Ref. [21]. In our work, we were using 10 iterations, each determined by a 8 ns transient simulation of the TWE model and a solution of the static problem (19) which takes around 4 min of CPU time in our case. The iterations of the thermally induced index $\Delta n_T(\bar{T})$, eq. (7), always converged rapidly within less than four iterations. Thereafter they fluctuated weakly around a constant level, which we interpreted as convergence. The fluctuations are consequence of the chaotic spatio-temporal dynamics.

5 Application I: Short-pulse operation

First we exemplary study an 10 ns long pulse by applying the NHF approximation at an injection current of 150 A, given by the total electric charge injected into the laser divided by the pulse length. High pulse powers with short pulse duration are for example utilized in light detection and ranging systems [22].

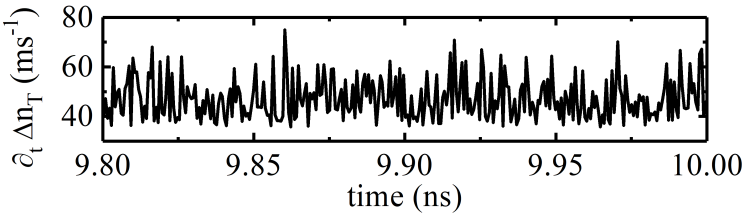

Figure 4: Thermal index generation rate of equation (18) during the last 200 ps of a 10 ns long 150 A current pulse transient.

The bias voltage U is instantaneously turned on and kept constant until it is switched of. After the turn on period, the thermal index generation rate under the stripe (Eq. (18)) is non-negative and strongly fluctuating around a mean value of about 50 ms^{-1} as shown in Fig. 4. Thus, the refractive index grows like a staircase. The individual steps, however, are typically only ps short and raise the index by less than 10^{-7}, so that their presence does not have an impact on the wave propagation.

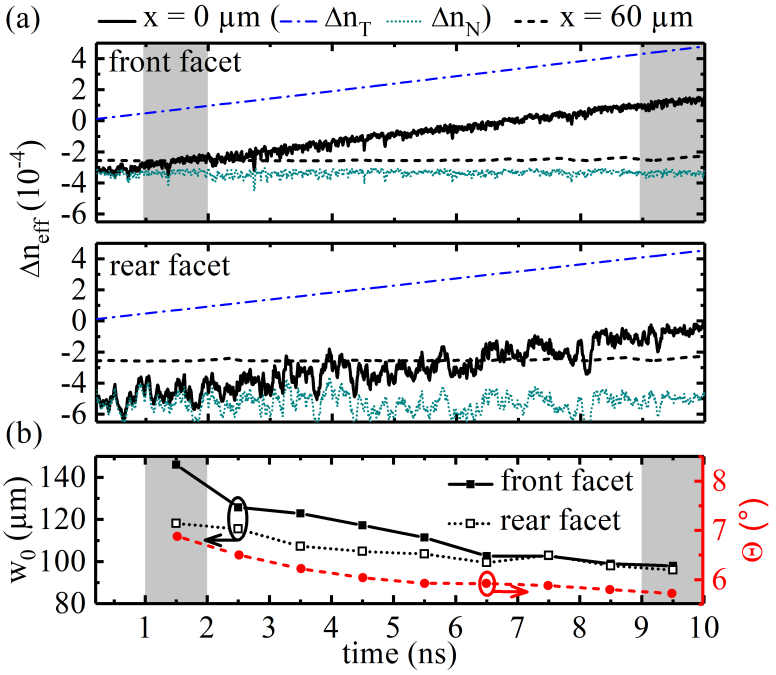

Figure 5: Thermal impact on waveguiding for a 10 ns long 150 A current pulse transient. (a) Effective index $\Delta n_{\text{eff}} = \Delta n_N + \Delta n_T$ below ($x = 0\,\mu$m) and beside the stripe ($x = 60\,\mu$m) at rear and front facet, respectively. Δn_T and Δn_N are also shown separately for $x = 0\,\mu$m. (b) Evolution of the near field widths (both facets) and far field width (front facet only), averaged over 1 ns (95% power content). Shadings: Time intervals used in the representations of Fig. 6.

The effective index rises below the stripe (black solid in Fig. 5(a)) due to the rising thermal contribution, whereas it remains approximately unchanged outside (black dashed). In this process, the index step

from outside to inside the stripe $\delta\Delta n_{\text{eff}} = \Delta n_{\text{eff}}(x = 0\,\mu\text{m}) - \Delta n_{\text{eff}}(x = 60\,\mu\text{m})$ rises from negative values immediately after turn on to positive values at the pulse end. At the time of transition, Fig. 6(a) shows the lateral profiles of Δn_N and Δn_T together for comparison, averaged over 1 ns. Here the effective index step $\delta\Delta n_{\text{eff}}$ from outside to inside the stripe nearly vanishes, whereas at the pulse end it is clearly positive forming a lateral waveguide as displayed in Fig. 6(b). In panels (c) and (d), the near field intensity, which is the forward propagating optical field intensity behind the front facet, and the far field intensity obtained from a Fourier transformation of the complex near fields, averaged over 1 ns, are shown. The disappearance of side wings in the near field and a change of the far field intensity are visible.

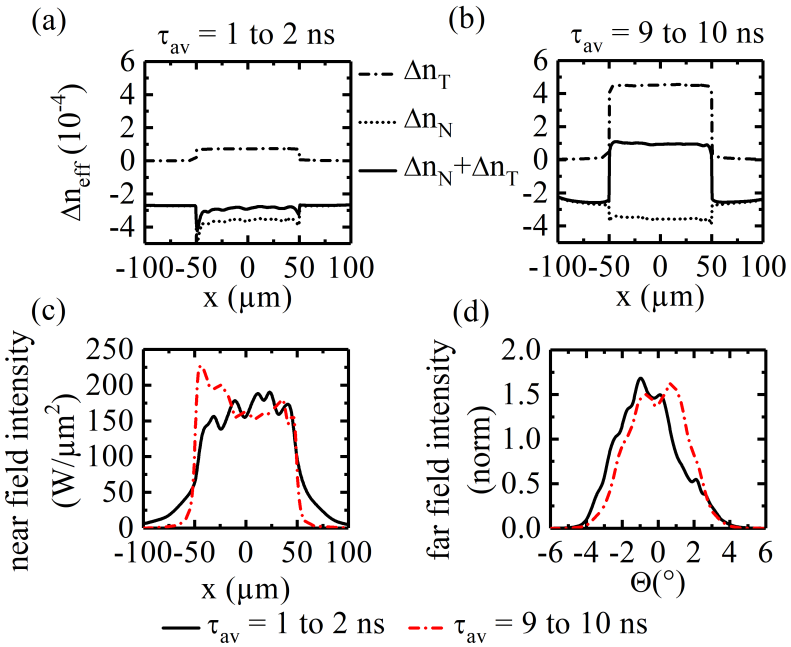

Figure 6: Thermal impact on waveguiding for a 10 ns long 150 A current pulse averaged over the pulse within the time interval 1 to 2 ns and 9 to 10 ns (gray shaded in Fig. 5(a) and (c)). (a) & (b) Lateral profiles of the effective index. (c) Near and (d) far field intensities at the front facet.

In laser structures with nonpositive index steps, lateral optical confinement results from the optical gain and accordingly this regime is usually called gain guided or anti-index guided. Operation regimes with positive index steps do not require the gain for optical confinement and are referred to as index guided. Thus, Fig. 5(a) indicates a transition from gain guiding to index guiding during the pulse. Such a transition has been reported already in [23] explaining long delay times for lasing of narrow-stripe lasers. Fig. 5(b) reveals that this transition is accompanied by a shrinking of both widths w_0 and Θ of the lateral near respective far fields, which improves the beam quality. Due to the longitudinal inhomogeneity, the transition happens at a later time near the rear facet, panel (a). It manifests itself in a narrower near field width at the rear facet at the pulse beginning due to stronger anti-guiding, panel (b).

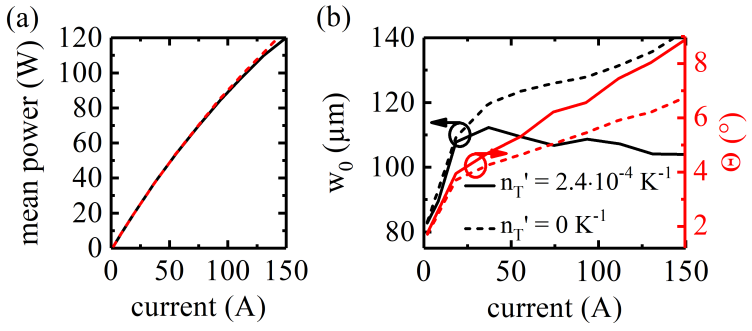

Figure 7: (a) Mean pulse power and (b) front facet near field width (black left axis) and far field angle (red right axis) containing 95 % of the power as function of mean pulse current for 10 ns long pulses with ($n'_{\text{T}} = 2.4 \cdot 10^{-4}$ K^{-1} - solid) and without ($n'_{\text{T}} = 0$ K^{-1} - dashed) thermal waveguiding, respectively.

The described formation of an initial thermally induced waveguide is also detectable in the dependence of time-averaged quantities on the pulse amplitude. Fig. 7(b) shows a shrinking of the near field width and increased far field angle with increasing injection current (solid curve), compared to the case without thermal waveguiding (dashed). The mean pulse power, given by the total pulse energy divided by the pulse length, as function of pulse current, in contrast, shows no dependence on waveguiding for currents up to 150 A as shown in Fig. 7(a). Note, that the neglected changes of parameters with temperature might have an additional influence.

The preceding results have been obtained neglecting heat flow. In order to check the validity of this approximation, we have performed the following post processing. We solve the full heat-flow Eq. (14) where the fluctuating heat source density h at each position is replaced by its average along the whole pulse. Moreover, we are disregarding heat flow in the (x, z)-plane and assume a vertically infinite domain with homogeneous material. This is justified because the extensions of lateral and longitudinal inhomogeneities in the heat source densities of the order of tens respective hundreds of micrometers (cf. Fig. 10) as well as the vertical size of the device are much larger than the expected heat spreading in the range of some hundred nanometers.

Under these conditions, the solution is (cf. Appendix C)

$$T(y,t) = \frac{1}{\sqrt{c_h \kappa_L}} \int_{-\infty}^{\infty} d\xi \; h(y+\xi) \; \sqrt{t} \; w\left(\frac{c_h \xi^2}{4\kappa_L t}\right), \tag{21}$$
$$\text{with } w(q) = \left\{ \sqrt{q}\,[\mathrm{erf}(\sqrt{q}) - 1] + \frac{1}{\sqrt{\pi}} e^{-q} \right\}.$$

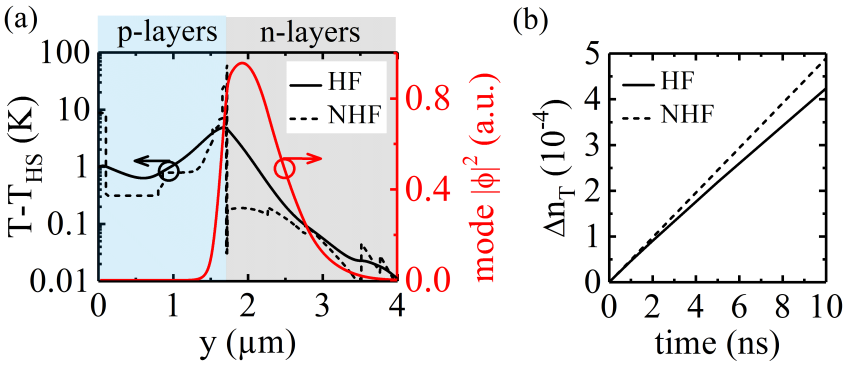

Figure 8: Impact of vertical heat flow for a 10 ns long 150 A current pulse. In all cases h is averaged over the pulse. (a) Black left axis: Vertical temperature profiles at the end of the 10 ns pulse (at front facet in the middle of the stripe). Black solid (HF): with heat flow, derived from Eq. (21). Black dashed (NHF): without heat flow. Red right axis: intensity profile of the vertical mode. (b) Thermally induced index (7) at the same position versus time. Black solid (HF): calculated from eq. (7) with $T(y,t)$ from eq. (21). Black dashed (NHF): without heat flow, calculated from eq. (18).

With increasing time, this function deviates more and more from the temperature increase $h(y)t$ without heat flow. Fig. 8(a) shows the situation in the stripe middle and at the pulse end. Here the vertical distribution of the temperature increase is displayed on the left axis. Heat flow reduces the excess temperature in the active layer from 60 K down to 5 K and smoothes the distribution considerably (solid line compared to dashed line). However, to derive the thermally induced index according to (7) the temperature profile has to be weighted with the intensity profile of the vertical mode $|\phi(y)|^2$ shown

in Fig. 8(a) on the right axis. Thus, irrespective of the large temperature differences obtained with and without heat flow, the thermally induced index differs only marginally between the two cases, Fig. 8(b).

One could think that the NHF approximation works nicely only for the special vertical mode profile shown in Fig. 8(a). However this is not the case; the profile belongs to a real-world high-power laser structure. The vertical intensity profiles of such lasers have to be wide to avoid facet damage and generally have a width of about one μm. The analysis presented here is actually already performed for an extremely asymmetric structure with a small overlap of the mode with the active region and the p-layers. For more symmetric structures the approximation works even better.

We will now come back to the experimental Fig. 2 in order to evaluate the model for short-pulse operation. The maximum wavelength shift there is $\Delta\lambda/\Delta t = 50$ pm/ns. With $\Delta\lambda/\Delta T = 0.33$ nm/K known from independent measurements, this corresponds to a temperature increase of $T = 1.5$ K in and around the active region for a 10 ns long 6.3 A current pulse. For 6.3 A the simulation yields temperature increases inside the active region of $T_{\mathrm{NHF}} = 4.1$ K and $T_{\mathrm{HF}} = 0.1$ K without and with vertical heatflow, respectively. Since the experimental value is below T_{NHF} but by a factor 15 larger than our best estimate T_{HF} and the used parameter values are known with significantly better precision, this suggests that the heat flow near the active region is inhibited by a mechanism not contained in the model. After estimating different possibilities, we regard the thermal boundary resistance (TBR) [24] of interfaces as the most probable one. Depending on the number of hetero-interfaces it could increase the temperature of the active region by some fractions of Kelvin [25]. Although the cause of inhibited heat transport remains unclear and is subject to further studies, it implies that the no-heat-flow approximation is even more realistic than expected.

6 Application II: CW operation

Whereas under pulsed operation the thermally induced waveguide is growing with increased time of excitation, under CW operation it approaches a steady state as discussed in section 4.2.2. Additionally to the much larger magnitude, under CW operation the effective index step below and beside the injection stripe, $\delta\Delta n_{\mathrm{eff}} = \Delta n_{\mathrm{eff}}(x = 0\,\mu\mathrm{m}) - \Delta n_{\mathrm{eff}}(x = 60\,\mu\mathrm{m})$, is a function of the longitudinal coordinate accompanied by a corresponding variation of the width of the lateral field intensity [7], too. This is exemplary displayed in Figs. 9(a) and (b) for a total injection current of $I \approx 19.5$ A and power at the output facet of $P_{\mathrm{out}} \approx 19$ W for the same structure discussed in the previous sections.

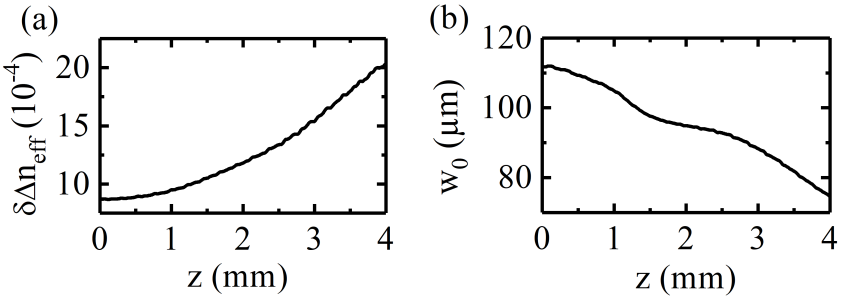

Figure 9: CW operation for $I \approx 19.5$ A and $P_{\mathrm{out}} \approx 19$ W. Time-averaged longitudinal evolution of (a) the effective index step below and beside the injection stripe, $\delta\Delta n_{\mathrm{eff}} = \Delta n_{\mathrm{eff}}(x = 0\,\mu\mathrm{m}) - \Delta n_{\mathrm{eff}}(x = 60\,\mu\mathrm{m})$ and (b) the width (95% power content) of the lateral field intensity.

The high asymmetry in the facet reflectivities gives rise to a strong z-dependence of the field intensity

and hence carrier density and Fermi potential due to longitudinal spatial holeburning [26]. This results in a z-dependence of all heat sources as displayed in Fig. 10. At this point of operation Joule and absorption heating have the highest fraction of the total heat production ($Q_{\text{Joule}} = 4.0$ W and $Q_{\text{abs}} = 3.9$ W compared to $Q_{\text{rec}} = 2.0$ W and $Q_{\text{defect}} = 1$ W) and as a result the temperature is higher at the front facet compared to the rear facet, Fig. 11(a).

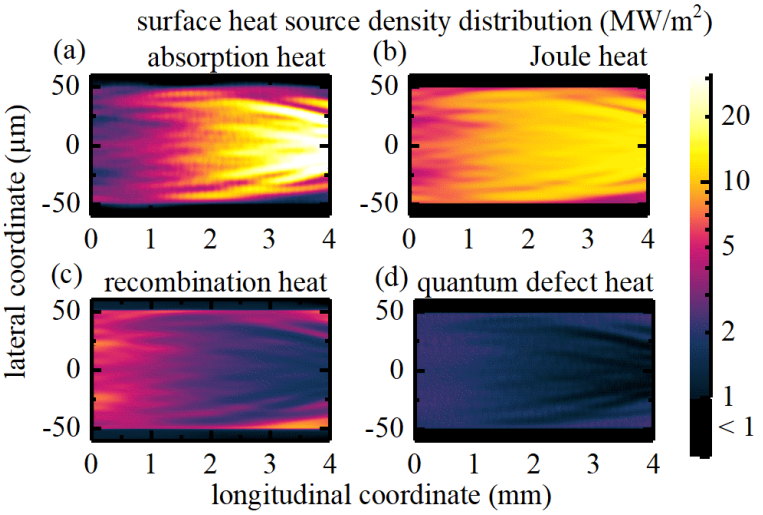

Figure 10: CW operation for $I \approx 19.5$ A and $P_{\text{out}} \approx 19$ W. Distribution of the time-averaged (a) absorption, (b) Joule, (c) recombination, and (d) quantum defect surface heat source densities $H = \int h dy$ as function of lateral and longitudinal (x, z)-coordinate.

At every time instance the field intensity distribution within the laser shows a fractured structure with small intensity peaks of longitudinal and lateral extent in the range of some micrometers, here exemplary shown for the forward propagating field u^+ in Fig. 11(c). The resulting highly dynamic behavior, which is inherent to broad-area lasers, is predicted by other simulation tools and has been experimentally verified [9, 27]. Spatial and temporal fluctuations of all heat source terms are the result. However, the fluctuating contribution to thermal waveguiding $\Delta n_{\text{T,fluct}}$ derived from Eq. (18) with $h_{\text{fluct}} = h - \bar{h}$ has a negligible influence on the results and can be disregarded under CW operation.

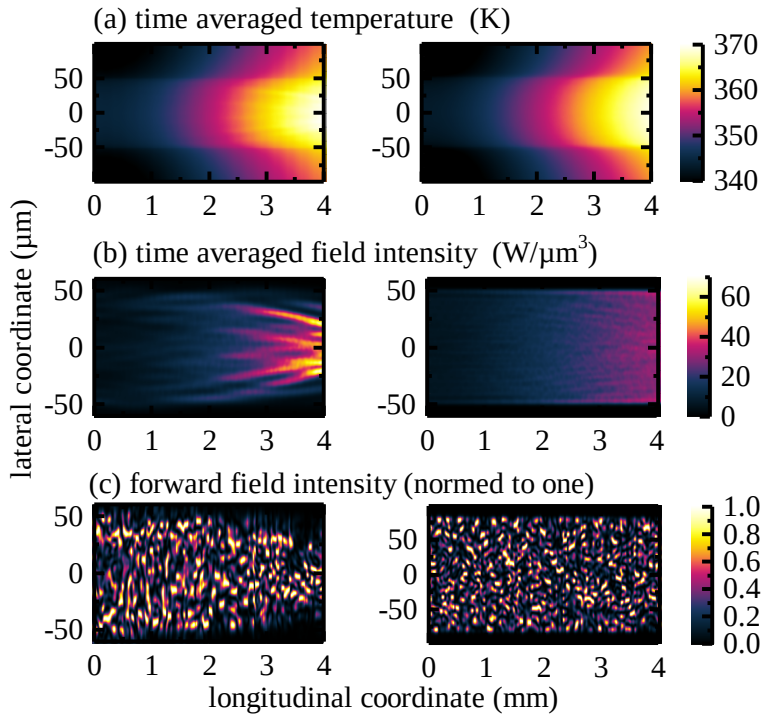

Figure 11: CW operation for $I \approx 19.5$ A and $P_{\text{out}} \approx 19$ W. (a) Time averaged temperature, (b) time averaged field intensity and (c) forward field intensity distribution at last time instance for the laser without (left) and with (right) trenches.

The temperature induced longitudinally varying index profile resulting in a narrowed optical field at the front facet is unfavorable, firstly because of the carrier accumulation at the stripe edges (visible in the gain profile in Fig. 12(a) and secondly because the enhanced power density lowers the threshold for facet damage.

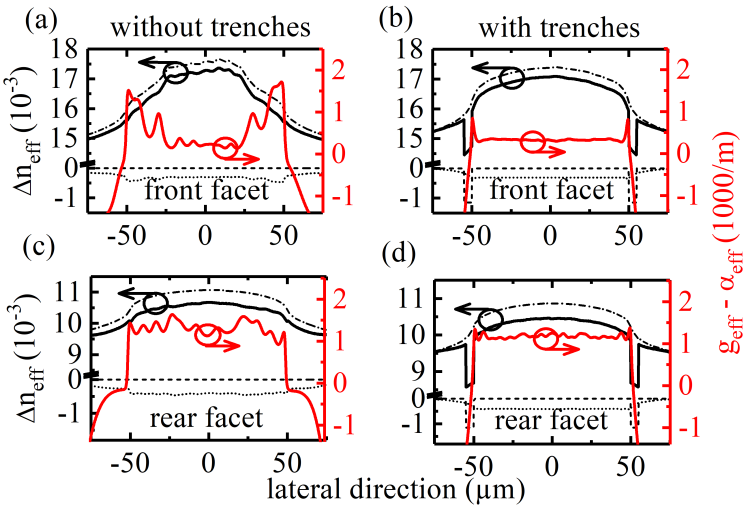

Figure 12: CW operation for $I \approx 19.5$ A and $P_{\text{out}} \approx 19$ W. Lateral profiles of the time averaged effective index and net gain at the front and rear facet for (a) & (c) the laser without and (b) & (d) with trenches. The non-solid black lines indicate the contributions due to etched index trenches (dashed line, Δn_0), temperature (dash-dotted line, Δn_T) and carrier density (dotted line, Δn_N).

To provide a temperature and carrier density independent lateral optical confinement, deep trenches filled with an insulator can be etched directly next to the injection stripe. Then the term $\Delta n_0(x)$ in (A.1) is negative at the trench position, see the black dashed line in the lateral profiles of the effective index in Figs. 12(b) and (d), where $\Delta n_0 = -1.15 \cdot 10^{-3}$ for $|x| \in [55 : 50]\,\mu$m. A comparison of the laser operation with and without trenches reveals, that although the temperature distribution remains largely unchanged, Fig. 11(a), the near field narrowing can be successfully counteracted by etching trenches, Fig. 11(b). Although the effective index is smaller at the rear compared to the front facet, the lateral effective index profile is stabilized by the trenches, Fig. 12(b) and (d). Accordingly also the gain function is laterally stabilized and remains box-shaped throughout the device with only small side peaks at the front facet. In contrast to this, the lateral gain and index profiles of the laser without trenches differ at the rear and front facet, Figs. 12(a) and (c).

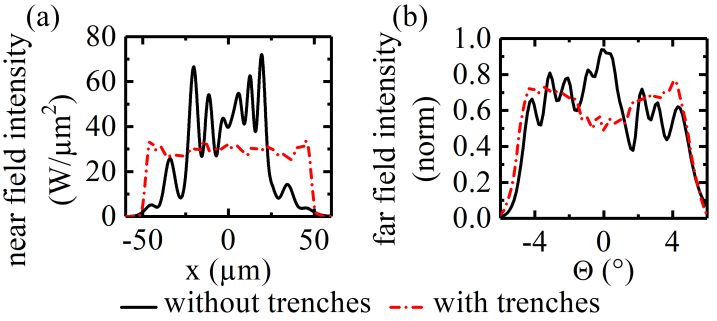

Figure 13: CW operation for $I \approx 19.5$ A and $P_{\text{out}} \approx 19$ W. (a) Near and (b) far field intensities of the laser without and with trenches.

The drawback of a laser design with etched trenches is a decreased beam quality, which is proportional to the widths of near and far field. In Fig. 13(a) it is visible that the lateral width of the emitted field is broadened to the width of the injection stripe. However, the profile of the far field remains nearly unchanged, see Fig. 13(b), and thus the beam quality is decreased. To suggest a reasonable design, it is necessary to counterbalance beam quality against efficiency and reliability.

Finally we compare our simulations with experimental results of a laser with a stripe width of $W = 90\,\mu$m, a cavity length of $L = 6$ mm and index trenches etched at $|x| \in [50 : 45]\,\mu$m ($\Delta n_0 = 3 \cdot 10^{-3}$). The measured and simulated power-current characteristics plotted in Fig. 14(a) show a good

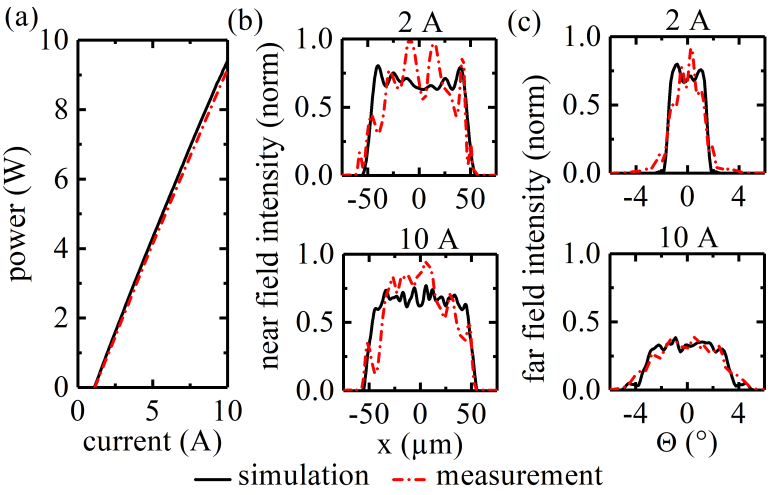

Figure 14: Measured and simulated (a) power-current characteristics, (b) near and (c) far fields for a laser with etched index trenches ($\Delta n_0 = 3 \cdot 10^{-3}$).

agreement. The widths of the near fields (Fig. 14(b)) remain almost constant if the current is increased from 2 A to 10 A as predicted in the preceding paragraph. Both the simulated and measured far fields (Fig. 14(c)) broaden with current. Although the overall behavior is correctly described by our simulation tool, the discrepancies concerning the multi-peaked structures of the fields necessitate further studies.

7 Conclusion and Outlook

We propose a physically realistic and yet numerically applicable thermal model to account for slow and fast temperature contributions in the time-dependent simulation of broad-area lasers. Although the temperature increase is small under pulsed operation, a waveguide that is introduced within a few-ns-long pulse can result in a transition from a gain-guided to an index-guided structure, leading to a near field narrowing. Heat flow is shown to have a marginal influence on this result. Comparing temperatures of the active zone calculated by the bulk heat-flow equations with measured ones, we find indications of an inhibition of heat flow by the possible thermal boundary resistance of hetero interfaces. For further improving the simulation model regarding pulsed applications it is therefore desirable to solve the time-dependent heat equation within a small vicinity of the active region $\approx 1\,\mu$m in vertical direction taking into account this boundary effect. Under continuous wave operation and for a laser with asymmetric facet reflectivities, the longitudinally varying temperature profile generated by unequal distributions of absorption and Joule heating at the facets is gained self-consistently. The resulting narrowing of the near field can be successfully counteracted by etching trenches.

Acknowledgment

This work has been supported by the German Federal Ministry of Education and Research (BMBF) contract 13N14005 as part of the EffiLas/HoTLas project. Furthermore we thank A. Pietrzak (JENOPTIK Optical Systems) for providing laser chips and K. Häusler and M. Beier for measurements.

Appendices

A Electro-optic parameters

Important properties of the optoelectronic model are given here, for more details see Ref. [11]. The optoelectronic part of the propagation parameter in Eq. (5),

$$\Delta\beta_{\mathsf{oe}}(N,\|u\|^2) = k_0\Delta n_0(x,z) + k_0\Delta n_N(N) + \frac{i}{2}\left[g_{\mathsf{eff}}(N,\|u\|^2) - \alpha_{\mathsf{eff}}(N)\right], \tag{A.1}$$

comprises built-in modifications of the effective index Δn_0 due to optionally etched trenches, carrier density N induced index contributions $\Delta n_N = -\sqrt{n'_N N}$. Furthermore it comprises gain $g_{\mathsf{eff}} = g' \ln(N/N_{\mathsf{tr}})/(1+\epsilon_{\mathsf{s}}\|u\|^2)$ and losses

$$\alpha_{\mathsf{eff}} = \alpha_{0,\mathsf{eff}} + f_N N + f_{\mathsf{2p}}(\|u\|^2 + |u^{\mp}|), \tag{A.2}$$

where $n'_N = 4.4\cdot 10^{-32}$ m^3, $g' = 1655$ m^{-1}, $N_{\mathsf{tr}} = 1.7\cdot 10^{24}$ m^{-3}, $\epsilon_{\mathsf{s}} = 6.6\cdot 10^{-26}$ m^3, $\alpha_{0,\mathsf{eff}} = 47$ m^{-1}, $f_N = 1.1\cdot 10^{-23}$ m^2, $f_{\mathsf{2p}} = 1.2\cdot 10^{-23}$ m^2 are the differential modal effective index, the differential modal gain, the transparency carrier density (obtained from a microscopic gain model [28] taking into account the QW confinement factor $\Gamma = 6.6\cdot 10^{-3}$ of the vertical mode), the gain compression factor (originating from a value of about 10^{-23} m^3, cf. [18], before multiplying with Γ), background absorption (free carrier absorption with cross sections of $4\cdot 10^{-22}$ m^2 for n-doped layers, $12\cdot 10^{-22}$ m^2 for p-doped layers [29]), the modal cross section for free-carrier absorption in the active region (obtained by fitting the slope of the power-current characteristics, corresponds to a total cross section of $16\cdot 10^{-22}$ m^2), and the modal two-photon absorption coefficient (originating from a typical value of $\beta = 14$ cm/GW, cf. [18], in the confinement and cladding layers properly weighted by the vertical mode profile), respectively. The dispersion operator,

$$\mathcal{D}u^{\pm} = \frac{g_r}{2}(u^{\pm} - p^{\pm}), \quad \frac{\partial p^{\pm}}{\partial t} = \gamma(u^{\pm} - p^{\pm}) + i\delta\omega p^{\pm}, \tag{A.3}$$

couples the TWE (2) to ordinary differential equations for the complex slowly varying amplitudes of the polarization fields $p^{\pm}$ [30]. This approximates the dispersion of the gain with a Lorentzian of amplitude g_r, half width at half maximum γ, and relative central frequency $\delta\omega$. The recombination rate,

$$R(N,\|u\|^2) = AN + BN^2 + CN^3 + R_{\mathsf{stim}}(N,\|u\|^2) \tag{A.4}$$

includes non-radiative and spontaneous radiative recombination with the coefficients for $A = 5\cdot 10^8$ s^{-1} (obtained by fitting the threshold current), $B = 1\cdot 10^{-16}$ m^{3}s^{-1} [20], and $C = 4\cdot 10^{-42}$ m^{6}s^{-1} [20] and the stimulated recombination $R_{\mathsf{stim}}(N,\|u\|^2) = v_g \mathsf{Re}\sum_{\nu=\pm} u^{\nu *}[g u^{\nu} - g_r(u^{\nu} - p^{\nu})]$.

B Thermoelectric effects

In this model vanishing Seebeck coefficients are assumed to avoid major alterations of the electric model and to maintain consistency at the same time. Furthermore in this way the heat equations are also valid in the non-Boltzmann case.

The price we pay is small: In the electronic model a feedback of temperature on the current (Seebeck effect), is neglected. However, as current conservation and charge neutrality must hold, this only

means slightly altered voltage gradients at hetero-boundaries and has no influence on the laser operation. In the heat models of [17, 18] due to non-vanishing Seebeck coefficients an extra term, the Thompson-Peltier heat source density, is considered. The main contribution of this heat term is generated near the active region, where current is injected into the QW passing a potential gradient from the free Fermi potential φ_F to the potential of bound states of the QW. In our model, this heat contribution is already accounted for in the defect heat term of Eq. (13) and the rest heat that is generated in the p- and n-layers is negligible.

C Solving the 1D Heat Flow Equation

Assuming constant c_h and κ_L, the one-dimensional Eq. (14) transforms to the standard heat equation

$$\frac{\partial T}{\partial t'} - \frac{\partial^2 T}{\partial y'^2} = h(\kappa_L y', c_h t') \tag{C.1}$$

by the substitutions $t = c_h t', y = \sqrt{\kappa_L} y'$. For initially $T = 0$, the solution is [31]

$$T(y', t') = \int_{-\infty}^{\infty} d\xi' \int_0^{t'} ds' h(\sqrt{\kappa_L}\xi', c_h s') H(y' - \xi', t' - s') \tag{C.2}$$

with the fundamental solution

$$H(\Delta y', \Delta t') = (4\pi\Delta t')^{-1/2} \exp\left\{-\frac{\Delta y'^2}{4\Delta t'}\right\}. \tag{C.3}$$

H is normalized to unity for any $\Delta t' > 0$. It drops rapidly down beyond the radius $\Delta y'^2 = \Delta t'$. With dimensions, this yields relation (17) for the ratio between elapsed time and radius of the spreading heat sphere. If the heat source h is time independent, the temporal integral in (C.2) can be performed analytically, yielding

$$T(y', t') = \sqrt{t'} \int_{-\infty}^{\infty} d\xi' \; h(\sqrt{\kappa_L}(y' + \xi')) w\left(\frac{\xi'^2}{4t'}\right). \tag{C.4}$$

Resubstituting $t' = t/c_h,\ y' = y/\sqrt{\kappa_L}$ and $\xi' = \xi/\sqrt{\kappa_L}$, we arrive at formula (21), where also $w(q)$ is given.

References

[1] P. Crump, S. Böldicke, C. M. Schultz, H. Ekhteraei, H. Wenzel, and G. Erbert, "Experimental and theoretical analysis of the dominant lateral waveguiding mechanism in 975 nm high power broad area diode lasers," *Semicond. Sci. Technol.*, vol. 27, pp. 045 001–1–9, 2012.

[2] G. R. Hadley, J. P. Hohimer, and A. Owyoung, "Comprehensive modeling of diode arrays and broad-area devices with applications to lateral index tailoring," *IEEE J. Quantum Electron.*, vol. 24, no. 11, pp. 2138–2152, 1988.

[3] L. Borruel, S. Sujecki, P. Moreno, J. Wykes, M. Krakowski, B. Sumpf, P. Sewell, S.-C. Auzanneau, H. Wenzel, D. Rodríguez, T. M. Benson, E. C. Larkins, and I. Esquivias, "Quasi-3-D simulation of high-brightness tapered lasers," *IEEE J. Quantum Electron.*, vol. 40, no. 5, pp. 463–472, 2004.

[4] J. Piprek, “Self-consistent analysis of thermal far-field blooming of broad-area laser diodes,” *Opt. Quantum Electron.*, vol. 45, no. 7, pp. 581–588, 2013.

[5] E. Gehrig and O. Hess, “Nonequilibrium spatiotemporal dynamics of the Wigner distributions in broad-area semiconductor lasers,” *Phys. Rev. A*, vol. 57, no. 3, pp. 2150–2162, 1998.

[6] K. Böhringer and O. Hess, “A full-time-domain approach to spatio-temporal dynamics of semiconductor lasers,” *Prog. Quantum Electron.*, vol. 32, pp. 159–246, 2008.

[7] S. Rauch, H. Wenzel, M. Radziunas, M. Haas, G. Tränkle, and H. Zimer, “Impact of longitudinal refractive index change on the near-field width of high-power broad-area diode lasers,” *Appl. Phys. Lett.*, vol. 110, no. 26, p. 263504, 2017.

[8] A. Klehr, H. Wenzel, O. Brox, S. Schwertfeger, R. Staske, and G. Erbert, “Dynamics of a gain-switched distributed feedback ridge waveguide laser in nanoseconds time scale under very high current injection conditions,” *Opt. Express*, vol. 21, no. 3, pp. 2777–2786, 2013.

[9] A. Klehr *et al*, “Pico- and nanosecond investigations of the lateral nearfield of broad area lasers under pulsed high-current excitation,” *Proc. SPIE*, vol. 10553, p. 105530K, 2018.

[10] M. Radziunas and R. Ciegis, “Effective numerical algorithm for simulations of beam stabilization in broad area semiconductor lasers and amplifiers,” *Math. Model. Anal.*, vol. 19, no. 5, pp. 627–646, 2014.

[11] A. Zeghuzi, M. Radziunas, H.-J. Wünsche, J.-P. Koester, H. Wenzel, U. Bandelow, and A. Knigge, “Traveling wave analysis of non-thermal far-field blooming in high-power broad-area lasers,” *IEEE J. Quantum Electron.*, vol. 55, no. 2, p. 2000207, 2019.

[12] BALaser, “A software tool for simulation of dynamics in broad area semiconductor lasers. http://www.wias-berlin.de/software/balaser/.”

[13] M. Radziunas, “Modeling and simulations of broad-area edge-emitting semiconductor devices,” *Int. J. High Perform. Comput. Appl.*, vol. 32, no. 4, pp. 512–522, 2018.

[14] M. Radziunas, A. Zeghuzi, J. Fuhrmann, T. Koprucki, H. J. Wünsche, H. Wenzel, and U. Bandelow, “Efficient coupling of the inhomogeneous current spreading model to the dynamic electro-optical solver for broad-area edge-emitting semiconductor devices,” *Opt. Quantum Electron.*, vol. 49, no. 10, 2017.

[15] A. Zeghuzi, H. Wenzel, H.-J. Wünsche, M. Radziunas, U. Bandelow, and A. Knigge, “Modeling of current spreading in high-power broad-area lasers and its impact on the lateral far field divergence,” *Proc. SPIE*, vol. 10526, p. 105261H, 2018.

[16] A. Othonos, “Probing ultrafast carrier and phonon dynamics in semiconductors,” *J. Appl. Phys.*, vol. 83, no. 4, pp. 1789–1830, 1998.

[17] U. Bandelow, H. Gajewski, and R. Hünlich, “Fabry-Pérot laser: Thermodynamics - based modeling of edge - emitting quantum well lasers,” in *Optoelectronic Devices - Advanced Simulation and Analysis*, J. Piprek, Ed. New York: Springer, 2005, ch. 3, pp. 63–85.

[18] H. Wenzel and A. Zeghuzi, “High-Power Lasers,” in *Handbook of Optoelectronic Device Modeling & Simulation*, 1st ed., J. Piprek., Ed. CRC Press, Taylor & Francis Group, 2017, ch. 33, pp. 15–58.

[19] J. Pomplun, H. Wenzel, S. Burger, L. Zschiedrich, M. R. Rozova, F. Schmidt, P. Crump, H. Ekhteraei, C. M. Schultz, and E. Götz, "Thermo-optical simulation of high-power diode lasers," *Proc. SPIE*, vol. 8255, p. 825510, 2012.

[20] J. Piprek, *Semiconductor Optoelectronic Devices*, 1st ed. San Diego: Academic Press, Elsevier, 2003.

[21] M. Radziunas, J. Fuhrmann, A. Zeghuzi, H.-J. Wünsche, T. Koprucki, C. Brée, H. Wenzel, and U. Bandelow, "Efficient coupling of dynamic electro-optical and heat-transport models for high-power broad-area semiconductor lasers," *Opt. Quantum Electron.*, vol. 51, no. 69, pp. 1–10, 2019.

[22] A. Knigge, A. Klehr, H. Wenzel, A. Zeghuzi, J. Fricke, A. Maaßdorf, A. Liero, and G. Tränkle, "Wavelength-stabilized high-pulse-power laser diodes for automotive LiDAR," *Phys. Status Solidi A*, vol. 215, no. 8, p. 1700439, 2018.

[23] F. C. Prince, T. J. S. Mattos, N. B. Patel, D. Kasemset, and C.-S. Hong, "Waveguiding, spectral, and threshold properties of a stripe geometry single quantum well laser," *IEEE J. Quantum Electron.*, vol. QE-21, no. 6, pp. 634–639, 1985.

[24] E. T. Swartz and R. O. Pohl, "Thermal boundary resistance," *Rev. Mod. Phys.*, vol. 61, no. 3, pp. 605–668, 1989.

[25] R. MacKenzie, J. J. Lim, S. Bull, Sujecki, and E. C. Larkins, "Inclusion of thermal boundary resistance in the simulation of high-power 980 nm ridge waveguide lasers," *Opt. Quantum Electron.*, vol. 40, pp. 373–377, 2008.

[26] A. J. Benett, R. D. Clayton, and J. M. Xu, "Above-threshold longitudinal profiling of carrier nonpinning and spatial modulation in asymmetric cavity lasers," *J. Appl. Phys.*, vol. 83, no. 7, p. 3784, 1998.

[27] I. Fischer, O. Hess, W. Elsäßer, and E. Göbel, "Complex spatio-temporal dynamics in the near-field of a broad-area semiconductor laser," *Europhys. Lett.*, vol. 35, no. 8, pp. 579–584, 1996.

[28] H. Wenzel, G. Erbert, and P. M. Enders, "Improved theory of the refractive-index change in quantum-well lasers," *IEEE J. Sel. Top. Quantum Electron.*, vol. 5, no. 3, pp. 637–642, 1999.

[29] M. Peters, V. Rossin, M. Everett, and E. Zucker, "High power, high efficiency laser diodes at JDSU," *Proc. SPIE*, vol. 6456, p. 64560G, 2007.

[30] C. Z. Ning, R. A. Indik, and J. V. Moloney, "Effective Bloch equations for semiconductor lasers and amplifiers," *IEEE J. Quantum Electron.*, vol. 33, no. 9, pp. 1543–1550, 1997.

[31] L. C. Evans, *Partial Differential Equations. Graduate Studies in Mathematics Vol. 19, Section 2.3*. American Mathematical Society, 1997.